

# Large-Area, Two-Dimensional MoS<sub>2</sub> Exfoliated on Gold: Direct Experimental Access to the Metal–Semiconductor Interface

Erik Pollmann,\* Stephan Sleziona, Tobias Foller, Ulrich Hagemann, Claudia Gorynski, Oliver Petri, Lukas Madauß, Lars Breuer, and Marika Schleberger



Cite This: *ACS Omega* 2021, 6, 15929–15939



Read Online

ACCESS |



Metrics & More

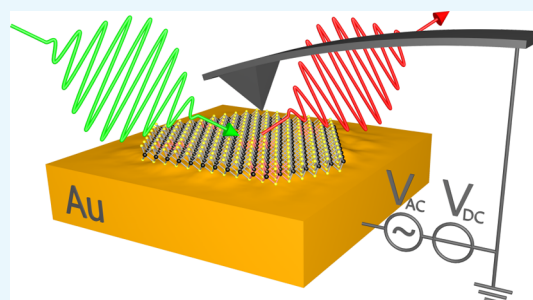


Article Recommendations



Supporting Information

**ABSTRACT:** Two-dimensional semiconductors such as MoS<sub>2</sub> are promising for future electrical devices. The interface to metals is a crucial and critical aspect for these devices because undesirably high resistances due to Fermi level pinning are present, resulting in unwanted energy losses. To date, experimental information on such junctions has been obtained mainly indirectly by evaluating transistor characteristics. The fact that the metal–semiconductor interface is typically embedded, further complicates the investigation of the underlying physical mechanisms at the interface. Here, we present a method to provide access to a realistic metal–semiconductor interface by large-area exfoliation of single-layer MoS<sub>2</sub> on clean polycrystalline gold surfaces. This approach allows us to measure the relative charge neutrality level at the MoS<sub>2</sub>–gold interface and its spatial variation almost directly using Kelvin probe force microscopy even under ambient conditions. By bringing together hitherto unconnected findings about the MoS<sub>2</sub>–gold interface, we can explain the anomalous Raman signature of MoS<sub>2</sub> in contact to metals [*ACS Nano*, 7, 2013, 11350] which has been the subject of intense recent discussions. In detail, we identify the unusual Raman mode as the A<sub>1g</sub> mode with a reduced Raman shift (397 cm<sup>-1</sup>) due to the weakening of the Mo–S bond. Combined with our X-ray photoelectron spectroscopy data and the measured charge neutrality level, this is in good agreement with a previously predicted mechanism for Fermi level pinning at the MoS<sub>2</sub>–gold interface [*Nano Lett.* 14, 2014, 1714]. As a consequence, the strength of the MoS<sub>2</sub>–gold contact can be determined from the intensity ratio between the reduced A<sub>1g, reduced</sub> mode and the unperturbed A<sub>1g</sub> mode.



## INTRODUCTION

Single-layer molybdenum disulfide (1L-MoS<sub>2</sub>), a semiconductor with a direct band gap in the visible spectrum,<sup>1–3</sup> is one of the most promising two-dimensional (2D) materials. Its characteristic electronic properties can be exploited for many applications such as field-effect transistors (FETs) as well as energy conversion, memory, and sensing devices.<sup>4–11</sup> These fields of application have one common aspect: the corresponding electrical devices require contacts to inject and extract charge carriers.

Such contacts constitute crucial interfaces for all electrical devices and are usually realized by metal–semiconductor junctions. For many applications, the aim is to minimize the height of the Schottky barrier often formed at these interfaces because this reduces the contact resistance and thus, for example, energy losses. The Schottky barrier height  $\phi_{\text{SBH}}$  of an n-type metal–semiconductor interface can be described by the following formula:<sup>12</sup>

$$\phi_{\text{SBH}} = S \cdot (\phi_{\text{m}} - \phi_{\text{CNL}}) + (\phi_{\text{CNL}} - \chi) \quad (1)$$

As shown in Figure 1, the metal work function  $\phi_{\text{m}}$ , the semiconductor electron affinity  $\chi$ , and the charge neutrality level  $\phi_{\text{CNL}}$  are referred to the vacuum level. The key parameter

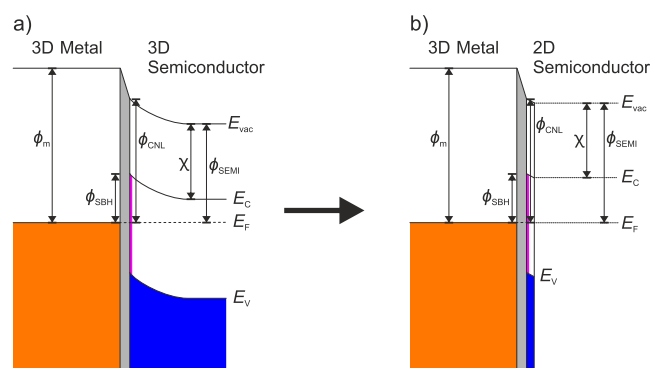


**Figure 1.** Fermi level pinned metal–semiconductor junction for (a) 3D metal and 3D semiconductor and (b) 3D metal and 2D semiconductor. Gray: interface region. Magenta: metal-induced gap or surface states.

Received: March 24, 2021

Accepted: May 6, 2021

Published: June 9, 2021



to describe the type of the Schottky barrier is the pinning factor  $S$ . For  $S = 1$ , the Schottky barrier height depends only on the metal work function  $\phi_m$  and the semiconductor electron affinity  $\chi$  (Schottky–Mott rule). If  $S = 0$ , the Fermi level of the semiconductor is completely pinned due to gap states at the metal–semiconductor interface. The resulting Schottky barrier height becomes independent from the metal and its work function but is rather determined by the charge neutrality level  $\phi_{\text{CNL}}$ :

$$\phi_{\text{SBH}_{\text{pinned}}} = \phi_{\text{CNL}} - \chi \quad (2)$$

The band structure for a classical junction between a 3D metal and a 3D semiconductor, which is strongly pinned by metal-induced gap and surface states (magenta), is shown in Figure 1a. These states define  $\phi_{\text{CNL}}$  at the semiconductor surface and thus  $\phi_{\text{SBH}}$ . The advantage of using the charge neutrality level  $\phi_{\text{CNL}}$  is that one does not require any details about the metal–semiconductor interface. Nevertheless, in order to experimentally investigate the mechanisms of the Schottky barrier formation, it is important to have access to the corresponding interface. Unfortunately, the interface in a 3D metal–3D semiconductor geometry is fully encapsulated by the two bulk materials.

However, in the case of 1L-MoS<sub>2</sub>, the semiconductor is thinned down to the lower limit resulting in a band structure as shown in Figure 1b. The opposite semiconductor surface is now extremely close to the inner interface, which allows to approximately characterize the inner metal–semiconductor interface from the surface side. For example, the measured work function of 1L-MoS<sub>2</sub>  $\phi_{\text{1L-MoS}_2}$  is close to its charge neutrality level ( $\phi_{\text{1L-MoS}_2} \approx \phi_{\text{CNL}}$ ).

Nevertheless, even for 2D materials like 1L-MoS<sub>2</sub>, the metal–semiconductor contact is usually experimentally characterized by one of the following three approaches: (i) “Black box”, which is a typical approach from the 3D semiconductor world. In this case, a parameter is changed (e.g., the metal of the contacts) and the response is measured (e.g., the contact resistance of a FET); (ii) characterization of 1L-MoS<sub>2</sub> decorated with metal particles; and (iii) characterization of the ideal MoS<sub>2</sub>–metal system, that is, grown by ultrahigh vacuum (UHV) epitaxy.

In particular, approach (i) is often used to determine the Fermi level pinning. The contact material is varied, and thus, the factor  $S$  can be derived. For MoS<sub>2</sub> with evaporated metal contacts, very low values of  $S$  are experimentally found, that is, MoS<sub>2</sub> in a typical device configuration has a strongly pinned Fermi level.<sup>13,14</sup>

Approach (ii) allows limited access by spectroscopic methods. Thereby, an anomalous Raman signature of MoS<sub>2</sub> (and WS<sub>2</sub>) after decoration with metal particles was observed,<sup>15–18</sup> which strongly differed from the expected Raman spectra for MoS<sub>2</sub>.<sup>19</sup> This anomaly manifests in a presumably strongly downshifted E<sub>2g</sub><sup>1</sup> mode and an additional mode next to the A<sub>1g</sub> mode with a lower wavenumber (at  $\sim 397$  cm<sup>-1</sup> for MoS<sub>2</sub>). The explanations offered for the altered Raman spectra are manifold: strong strain due to the gold contact and enhancement by surface plasmons,<sup>15–17</sup> a change in the polarization direction of the excitation by plasmon excitation,<sup>16</sup> and plasmon–phonon coupling,<sup>18</sup> respectively. Because of the indirect experimental access, these explanations remain incomplete and/or insufficiently corroborated. For example, although the E<sub>2g</sub><sup>1</sup> mode position is strongly affected by

strain and may even split,<sup>20–22</sup> this has never been observed for the A<sub>1g</sub> mode.

Finally, approach (iii) grants access to ideal systems. The substrate is in this case typically an ultraclean single crystal (SC), and the growth proceeds via molecular beam epitaxy under UHV conditions. Such a perfect, textbook system provides fundamental insights, but these are hardly transferable to real, imperfect systems.

Thus, while all these approaches yield important information about the interface, they share one major drawback: they do not access a real metal–semiconductor interface of a device, which typically consists of a non-perfect metal grown by physical vapor deposition (PVD) in contact with the semiconductor. Therefore, so far, it is mainly theoretical models that provide access to the physical properties and processes at the interface, and experimental data are scarce.<sup>23–29</sup>

We solve this problem by establishing a novel experimental approach to the metal–semiconductor interface of real devices. We achieve this by large-area exfoliation of 1L-MoS<sub>2</sub> on polycrystalline gold (Au).<sup>30–32</sup> This preparation method does not require a perfect single-crystalline gold surface as in UHV epitaxy but only a particularly clean gold surface. This type of gold surface can be produced by PVD methods typically used in lithography techniques, resulting in junctions similar to those found in devices. The major advantage is that 1L-MoS<sub>2</sub> is located on top of the gold layer and is still atomically thin. Therefore, the 2D material and its interface to the metal are both available for direct characterization, which we demonstrate in our paper. By measuring the 1L-MoS<sub>2</sub> work function  $\phi_{\text{1L-MoS}_2}$ , the charge neutrality level  $\phi_{\text{CNL}}$  at the MoS<sub>2</sub>–Au interface and, hence, the Schottky barrier height  $\phi_{\text{SBH}}$  (according to eq 2 for the strongly pinned MoS<sub>2</sub>–Au contact<sup>13,14</sup>) can now be studied.

In order to understand the nature of the MoS<sub>2</sub>–metal contact, we combine large-area exfoliated 1L-MoS<sub>2</sub> on Au with surface characterization techniques such as atomic force microscopy (AFM), particularly Kelvin probe force microscopy (KPFM), Raman spectroscopy, and X-ray photoelectron spectroscopy (XPS).

Our paper provides experimental evidence for a theoretically predicted mechanism of a sulfur-mediated gap state arising from molybdenum d-orbitals at the MoS<sub>2</sub>–Au interface affecting the Fermi level pinning.<sup>25</sup> We find that both  $\phi_{\text{CNL}}$  measured by KPFM and the intensity of the anomalous Raman signature depend on the smoothness of the Au surface and thus on the MoS<sub>2</sub>–Au contact strength. While the KPFM data are linked to Fermi level pinning, we explain the mysterious Raman signature of the first MoS<sub>2</sub> layer on gold by an elementary description of the Raman modes, which is corroborated by our XPS data. Although we cannot exclude the existence of exotic quasiparticles, we show that it is not necessary to introduce them as an explanation for the Raman signature. Instead, we argue that it has its origin in the metal-induced gap states that also cause the predicted pinning of the Fermi level.

## RESULTS AND DISCUSSION

We begin by explaining our sample preparation. We took great care to prepare clean interfaces and to minimize contaminations from ambient conditions. An exemplary sample from the exfoliation of MoS<sub>2</sub> on a freshly prepared 25 nm Au film

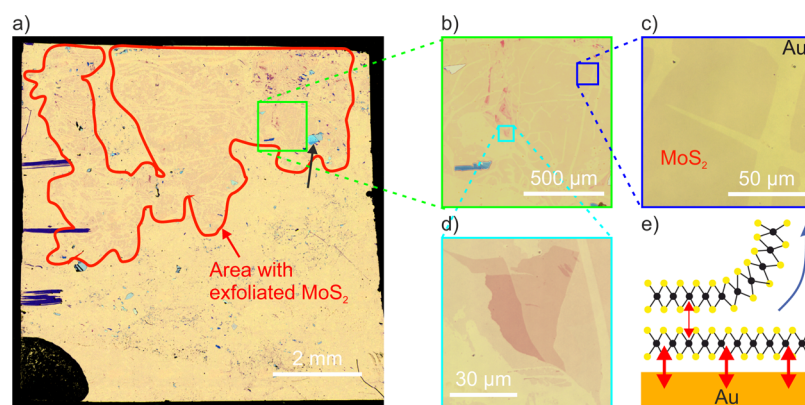


**Figure 2.** Large-area exfoliation of MoS<sub>2</sub> on a freshly prepared gold surface. (a–d) Optical microscopy images with different magnifications provide both overview and details of the sample. (e) Schematic illustration of the mechanism of large-area exfoliation caused by the strong interaction (symbolized by red arrows) between the gold surface and the first MoS<sub>2</sub> layer in direct contact with the surface. In order to improve the visibility, the images have been edited afterward.

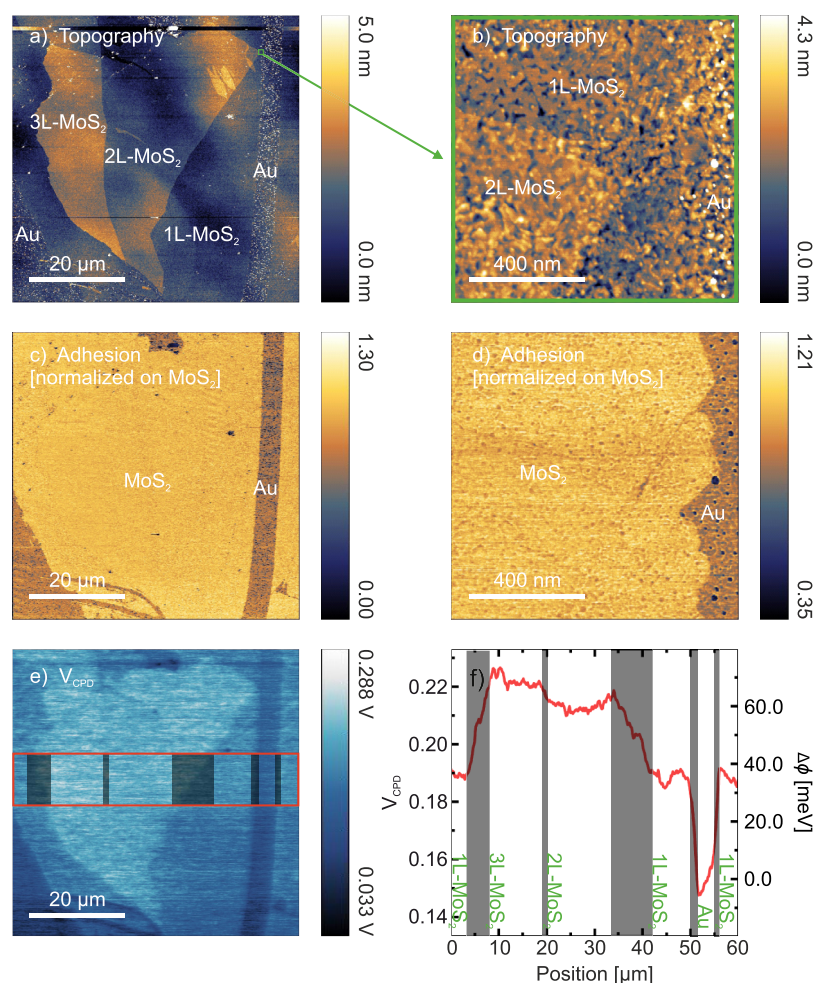


**Figure 3.** PeakForce KPFM measurements of MoS<sub>2</sub> exfoliated onto a 25 nm PVD-Au film (the same flake as in Figure 2d). (a) Topography, (c) adhesion, and (e)  $V_{\text{CPD}}$  image of a large-area scan. (b) Topography and (d) adhesion image of a zoom [green marked area in (a)]. (f) Averaged line scans of the area marked in red along the fast scan direction in (e) showing the measured  $V_{\text{CPD}}$  values for Au, 1L-, 2L-, and 3L-MoS<sub>2</sub> and the respective work function difference with respect to the Au level.

grown by PVD on SiO<sub>2</sub> is shown in Figure 2. The overview of the entire sample in Figure 2a demonstrates the successful large-area exfoliation: in the several mm<sup>2</sup>-sized regions marked in red, large areas with homogeneous optical contrast can be seen, which differs from the gold surface contrast. These are

the 1L-MoS<sub>2</sub> areas. A few smaller bulk-like MoS<sub>2</sub> crystallites are also visible on the gold surface, which are typical for exfoliation and have a vertical dimension of a few 100 nm (black arrow). The enlargements in Figure 2b–d improve the visibility of the homogeneous 1L-MoS<sub>2</sub> areas and occasional

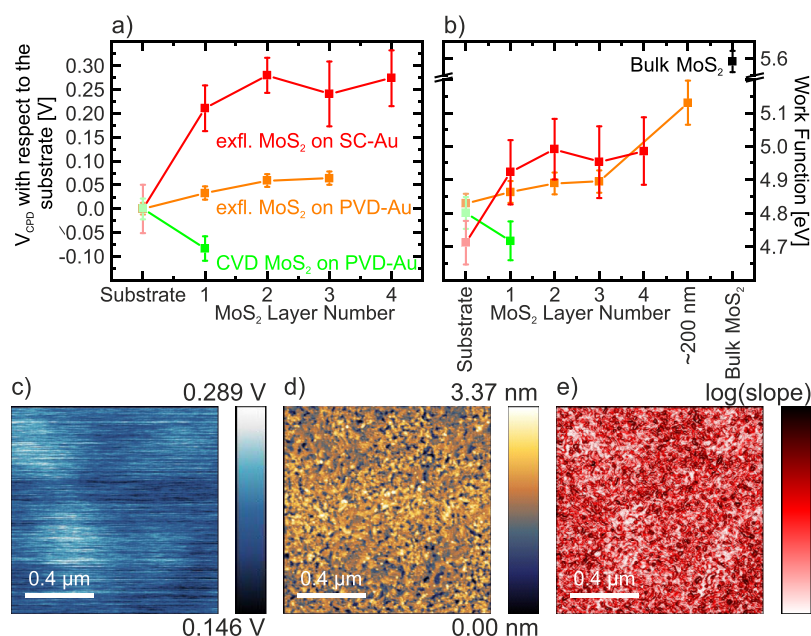


**Figure 4.** Substrate and MoS<sub>2</sub> layer number-dependent KPFM data of differently prepared MoS<sub>2</sub>-Au samples. (a)  $V_{\text{CPD}}$  of exfoliated MoS<sub>2</sub> on 25 nm PVD-Au (orange) and on SC-Au (red) and of CVD MoS<sub>2</sub> transferred on 25 nm PVD-Au (green) with respect to the surrounding substrate level. (b) Respective work function after tip calibration. (c)  $V_{\text{CPD}}$ , (d) topography, and (e) local slope (logarithmic) image of 1L-MoS<sub>2</sub> exfoliated on 25 nm PVD-Au revealing a correlation between work function and Au surface smoothness.

few-layer areas. In Figure 2d, 2L-MoS<sub>2</sub> and 3L-MoS<sub>2</sub> are distinguishable by their increasing contrast.

In general, mechanical exfoliation of 2D materials is explained by an adhesive force between the substrate surface and the top 2D material layer of the crystallite attached to the scotch tape. Therefore, to isolate a single layer of MoS<sub>2</sub> over such large areas on gold, this force must be much stronger than the interlayer van der Waals force between individual MoS<sub>2</sub> layers; see illustration in Figure 2e. Because large-area MoS<sub>2</sub> exfoliation on gold has been previously only observed on freshly produced gold surfaces—after a few minutes in air, natural contaminations prevent an immediate MoS<sub>2</sub>-Au contact—<sup>30,31</sup> the strong adhesive force between MoS<sub>2</sub> and gold is attributed to an extraordinary MoS<sub>2</sub>-Au interaction. We can qualitatively confirm this observation (Figure 2) and additionally demonstrate that a Au(111) SC surface can be sufficiently cleaned by standard surface science techniques to allow large-area MoS<sub>2</sub> exfoliation; see the Supporting Information, Figure S4.

For a more detailed characterization of our sample, we apply AFM and particularly KPFM to access the work function via the contact potential difference ( $V_{\text{CPD}}$ ). Figure 3 shows a  $V_{\text{CPD}}$  mapping obtained by KPFM under ambient conditions and simultaneously measured topography and adhesion images of the flake shown in Figure 2d. Based on the topography image in Figure 3a, the second and third MoS<sub>2</sub> layers can easily be identified. The magnification of a MoS<sub>2</sub>-Au edge (Figure 3b) shows the peculiarity that in this channel, the first MoS<sub>2</sub> layer cannot be distinguished from the Au surface as no step is found. In the topography, only small particles on the Au surface provide an indication of where Au and where MoS<sub>2</sub> are located, respectively. The adhesion channel shown in Figure 3c,d helps to solve this problem as it provides a significant material contrast. By comparing both channels—topography and adhesion—with the  $V_{\text{CPD}}$  mapping (Figure 3e) and the corresponding line scans (Figure 3f), areas can unambiguously

be assigned to the MoS<sub>2</sub> layer numbers and the gold substrate, respectively. The line scan in Figure 3f shows the average of 100 parallel profiles within the red box of Figure 3e. The grayed areas are the transitional areas due to steps. An increasing  $V_{\text{CPD}}$  value with increasing MoS<sub>2</sub> layer number becomes visible.

In order to study the influence of the substrate on the work function, we used three different types of samples and measured  $V_{\text{CPD}}$  with respect to the substrate  $V_{\text{CPD}}$ : (i) exfoliated MoS<sub>2</sub> on a 25 nm Au film prepared by PVD (orange), (ii) exfoliated MoS<sub>2</sub> on SC-Au (red), and (iii) chemical vapor deposition (CVD)-grown MoS<sub>2</sub> transferred onto a 25 nm PVD-Au film (green). The result is shown in Figure 4a. See the Supporting Information, Figure S4, for additional KPFM images. By calibrating the used AFM tips on freshly cleaved highly oriented pyrolytic graphite (HOPG,  $\phi = 4.62 \pm 0.02$  eV<sup>33</sup>), the corresponding work functions can be determined. This leads to the diagram shown in Figure 4b. To complete the data set, the two data points for ~200 nm thick, bulk-like MoS<sub>2</sub> on Au and for the freshly cleaved bulk MoS<sub>2</sub> used for the exfoliation are included.

The increasing work function with increasing layer number observed for MoS<sub>2</sub> exfoliated on 25 nm PVD-Au (Figures 3e,f and 4b) is typical for MoS<sub>2</sub> as bulk MoS<sub>2</sub> is a high work function material and is accordingly relatively p-doped compared to 1L-MoS<sub>2</sub>.<sup>34–39</sup> Because the electronic structure of MoS<sub>2</sub> strongly changes within the first few layers,<sup>1–3</sup> it is difficult to transfer models of the classical metal–semiconductor contacts to the MoS<sub>2</sub>-Au system with varying MoS<sub>2</sub> layer numbers. Therefore, only 1L-MoS<sub>2</sub> will be discussed in the following.

For the three different sample systems, we find the following work functions of 1L-MoS<sub>2</sub>: (i)  $\phi_{\text{exfl.MoS}_2\text{-PVD-Au}} = 4.864 \pm 0.033$  eV, (ii)  $\phi_{\text{exfl.MoS}_2\text{-SC-Au}} = 4.923 \pm 0.096$  eV, and (iii)  $\phi_{\text{CVD-MoS}_2\text{-PVD-Au}} = 4.718 \pm 0.058$  eV. Apparently, transferred

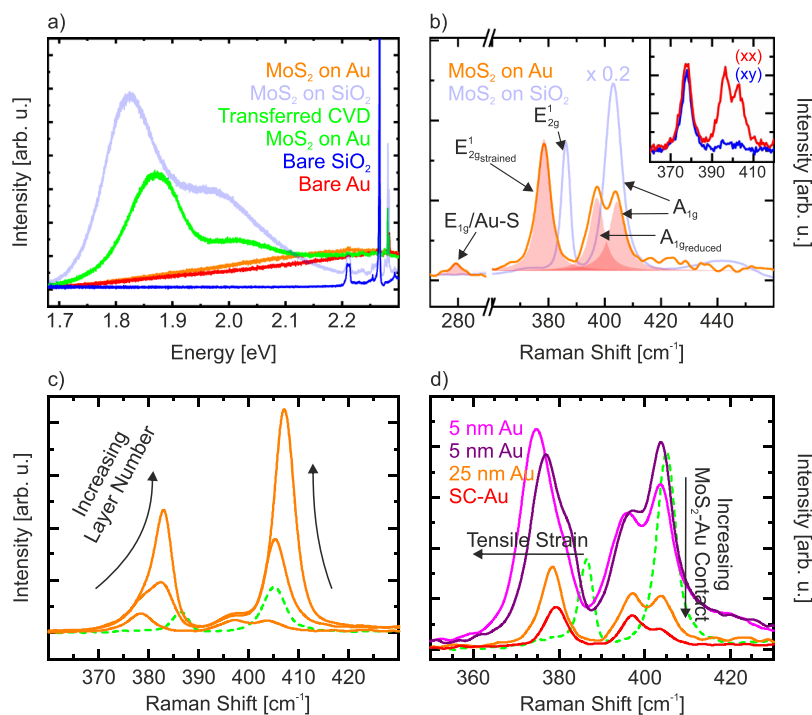


**Figure 5.** PL and Raman spectra of MoS<sub>2</sub> on Au and on SiO<sub>2</sub>. (a) Strong PL quenching of 1L-MoS<sub>2</sub> exfoliated on Au (orange) in comparison to the spectra measured for 1L-MoS<sub>2</sub> exfoliated on SiO<sub>2</sub> (light blue), CVD 1L-MoS<sub>2</sub> transferred on Au (green), bare Au (red), and bare SiO<sub>2</sub> (blue). (b) Altered Raman spectra of 1L-MoS<sub>2</sub> exfoliated on Au in contrast to MoS<sub>2</sub> exfoliated on SiO<sub>2</sub>. Inset: polarization-dependent Raman spectra of 1L-MoS<sub>2</sub> exfoliated on Au revealing the additionally emerging A<sub>1g</sub><sup>reduced</sup> mode to be an A-type Raman mode. (c) Layer (1L-, 2L-, and 3L-MoS<sub>2</sub> exfoliated on 25 nm PVD-Au) and (d) substrate (5 nm PVD-Au, 25 nm PVD-Au, and SC-Au)-dependent Raman spectra. Green spectra: CVD 1L-MoS<sub>2</sub> transferred on 25 nm Au. Magenta: 1L-MoS<sub>2</sub> exfoliated on 5 nm Au. Purple: 1L-MoS<sub>2</sub> exfoliated on 5 nm Au after water intercalation (more information in the Supporting Information, Figure S5).

CVD MoS<sub>2</sub> is relatively n-doped—in this case, the contrast to gold in the  $V_{\text{CPD}}$  image is even inverted (see the Supporting Information, Figure S4). The fabrication method can be excluded as explanation for the low work function (and the differing Raman signature discussed further below) of CVD-grown MoS<sub>2</sub>. We reported previously that CVD MoS<sub>2</sub> transferred onto SiO<sub>2</sub> behaves very similar (e.g., exhibiting a non-differing doping level) to MoS<sub>2</sub> exfoliated onto SiO<sub>2</sub> with intercalated water.<sup>40</sup> Hence, the major difference between exfoliated and CVD MoS<sub>2</sub> is the (de)coupling to (from) the substrate. The decisive factor for the work function is the MoS<sub>2</sub>–Au contact. Previous studies have shown that MoS<sub>2</sub> becomes p-doped after Au or Ag nanoparticle decoration.<sup>41,42</sup> Because transferred CVD MoS<sub>2</sub> has no direct contact to the gold surface but together with the gold substrate encloses a buffer layer of airborne contaminations and water, it is found to be relatively n-doped.

Our findings are further corroborated by the remaining photoluminescence (PL) in the case of transferred CVD MoS<sub>2</sub>, while it is strongly quenched for exfoliated MoS<sub>2</sub> on Au, as seen in Figure 5a. Quenching of the PL is attributed to a charge transfer between MoS<sub>2</sub> and Au<sup>43</sup> leading to an efficient exciton dissociation and is thus an obvious indicator for a good MoS<sub>2</sub>–Au contact. Therefore, our reference system based on transferred CVD MoS<sub>2</sub> is indeed decoupled from the Au substrates, while exfoliated MoS<sub>2</sub> interacts electronically with the differently prepared Au surfaces.

The PL data and the  $V_{\text{CPD}}$  data of 1L-MoS<sub>2</sub> exfoliated on the two different Au surface types indicate that the 2D material is to some degree in direct contact with the metal substrate. The

increase in work function is expected for Fermi level pinning as pinning shifts the Fermi level toward the middle of the band gap at 4.95–5.25 eV (based on a 1L-MoS<sub>2</sub> electron affinity of 4.0–4.3 eV and a band gap of  $\sim 1.9$  eV<sup>1–3,25,44–46</sup>). According to eq 2, for a strongly pinned metal–semiconductor interface, we can conclude that the Schottky barrier of 1L-MoS<sub>2</sub> on SC-Au is about 60 meV higher than that on 25 nm PVD-Au. This can simply be explained by the morphology of SC-Au. Its smooth surface provides a larger contact area where a true metal–semiconductor interface indeed exists, and hence, the density of gap states is higher. This is further confirmed by spatial  $V_{\text{CPD}}$  inhomogeneities of 1L-MoS<sub>2</sub> on PVD-Au shown in Figure 4c. The increased  $V_{\text{CPD}}$  values clearly correlate with smooth areas in the topography (Figure 4d), which can be better visualized by a reduced local slope density of the topography (Figure 4e). In contrast to PVD-Au, we observe nanobubbles for MoS<sub>2</sub> on SC-Au;<sup>32</sup> see the Supporting Information, Figure S4e,f. In areas of higher bubble densities in the MoS<sub>2</sub> layer (less strong MoS<sub>2</sub>–Au interactions), we measure a lower work function than in areas of lower bubble densities (strong MoS<sub>2</sub>–Au interactions). This correlation between bubble density, MoS<sub>2</sub>–Au interactions, and work function also confirms our interpretation. Furthermore, it explains the larger error bars of the measured work function for MoS<sub>2</sub> on SC-Au and thus superimposes the dependence on the number of layers (Figure 4a,b).

Fermi level pinning is attributed to gap states at the metal–semiconductor interface, which are typically formed by surface defects, chemical bonds between the metal and semiconductor, or metal-induced states at the interface. In order to examine

the origin of gap states in the MoS<sub>2</sub>–Au system, we analyze our sample by means of Raman spectroscopy and XPS and show in the following that the degree of contact area of MoS<sub>2</sub> on Au surfaces also correlates with spectroscopic data, which can be interpreted as Mo–S bond softening.

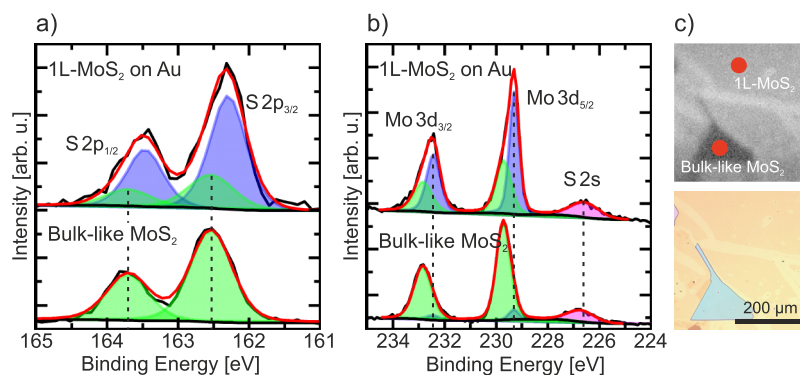
Raman measurements of 1L-MoS<sub>2</sub> exfoliated on Au display an anomalous spectrum for MoS<sub>2</sub> (Figure 5b), which exhibits features similar to spectra previously found for MoS<sub>2</sub> (and WS<sub>2</sub>) decorated with metallic nanoparticles.<sup>15–17</sup> The most prominent peaks are still close to the typical MoS<sub>2</sub> modes around 400 cm<sup>-1</sup>—as a reference, the Raman spectrum of MoS<sub>2</sub> exfoliated on SiO<sub>2</sub> is shown (blue)—but they are strongly shifted or split, or additional peaks appear, while the intensities of other peaks are reduced. These characteristics are highly unusual and are not compatible with known defect-induced changes in the Raman spectrum.<sup>47–49</sup> Although even small defect densities are predicted to strongly affect the Fermi level at the MoS<sub>2</sub>–metal interface,<sup>26,50</sup> this cannot explain the anomalous Raman spectra.

Figure 5c,d shows that the appearance of additional Raman modes around 379 and 397 cm<sup>-1</sup> (the latter is referred to as the A<sub>1g, reduced</sub> mode in the following) is a first-layer effect that only occurs for MoS<sub>2</sub> in direct contact with the Au surface. By increasing the layer number, the normal Raman modes increase in intensity, while the additional modes remain almost constant in intensity and position as shown in Figure 5c. Beginning with the second MoS<sub>2</sub> layer, the typical E<sub>2g</sub><sup>1</sup> and A<sub>1g</sub> modes become dominant and shift apart with increasing layer number as known for few-layered MoS<sub>2</sub>.<sup>19</sup> Figure 5d demonstrates that the Raman spectra are strongly dependent on the quality of the contact between 1L-MoS<sub>2</sub> and the Au surface. The mode around 379 cm<sup>-1</sup> can be interpreted as the E<sub>2g</sub><sup>1</sup> mode of strained MoS<sub>2</sub>. Tensile strain shifts the E<sub>2g</sub><sup>1</sup> mode to lower wavenumbers and in extreme cases even splits the mode.<sup>20–22</sup> This strain effect agrees well with the smoothness of the Au surfaces used here. We find 1L-MoS<sub>2</sub> to be most strained on 5 nm PVD-Au, which is a non-continuous, rough Au surface (Figure 5d, magenta). As the PVD-Au film closes at a nominal thickness of 25 nm, the strain is reduced (Figure 5d, orange). On the smoothest SC-Au surface, 1L-MoS<sub>2</sub> is most relaxed (Figure 5d, red). Topography images taken by AFM of the respective PVD-Au surfaces confirming this correlation can be found in the Supporting Information, Figure S3. With increasing smoothness of the Au surface, the intensity ratio A<sub>1g, reduced</sub>/A<sub>1g</sub> increases. Therefore, it is evident that the emergence of the A<sub>1g, reduced</sub> mode around 397 cm<sup>-1</sup> is caused by the direct MoS<sub>2</sub>–Au contact.

The analysis of the Raman spectra is further confirmed by 1L-MoS<sub>2</sub> on 5 nm PVD-Au intercalated with water (Figure 5d, purple) and transferred CVD 1L-MoS<sub>2</sub> on 25 nm PVD-Au (Figure 5d, green). If water intercalates underneath exfoliated MoS<sub>2</sub>, the latter relaxes (the E<sub>2g</sub><sup>1</sup> mode shifts to higher wavenumbers) and its degree of contact is reduced (the A<sub>1g, reduced</sub>/A<sub>1g</sub> mode ratio decreases). More information and optical microscopy images are available in the Supporting Information, Figure S5. For transferred CVD MoS<sub>2</sub> on PVD-Au, we find the typical Raman signature of 1L-MoS<sub>2</sub> with its two characteristic peaks. This can again be explained by a continuous and thick buffer layer of contaminations and water existing between the transferred MoS<sub>2</sub> layer and the Au surface, which prevents the direct MoS<sub>2</sub>–Au contact and hence a strong MoS<sub>2</sub>–Au interaction.

Note that the different absolute intensities in Figure 5b,d are attributed to interference effects due to the underlying SiO<sub>2</sub> layer<sup>19</sup> and its screening by the metal layers. Because CVD MoS<sub>2</sub> transferred onto 25 nm PVD-Au is not in direct contact to the Au surface and thus its Raman signature is not changed, the intensity reduction caused exclusively by the screening of the interference effects can be quantified with this system. In comparison to 1L-MoS<sub>2</sub> on SiO<sub>2</sub>—exfoliated as well as grown by CVD—the intensity (sum of the peak areas of the characteristic MoS<sub>2</sub> modes) of CVD 1L-MoS<sub>2</sub> on 25 nm PVD-Au is reduced to ~25%. The alteration of the Raman signature due to the direct contact of 1L-MoS<sub>2</sub> exfoliated on 25 nm PVD-Au further reduces the intensity to ~19%. Because of the reduced Raman intensity of MoS<sub>2</sub> on gold, a study of the dependency on the power density and the energy density (via the integration time) was performed on 1L-MoS<sub>2</sub> exfoliated on gold to determine appropriate parameters for Raman spectroscopy (see Figure S8). In this way, laser parameters are determined that provide a sufficient signal-to-noise ratio and do not significantly alter or damage the MoS<sub>2</sub> surface. It also shows that the unusual Raman signature is not a result of the increased incident energy densities necessary to record the spectra with a sufficient signal-to-noise ratio.

We have provided ample experimental evidence that the appearance of the altered Raman spectrum depends on the quality of the contact between the first MoS<sub>2</sub> layer and the Au substrate. In the following, we will focus on the hitherto unexplained origin of the A<sub>1g, reduced</sub> mode around 397 cm<sup>-1</sup>. We propose that it is directly related to the MoS<sub>2</sub>–Au interaction and will give a straight-forward explanation for the interconnection between the electronic states and the phonon modes. Because the appearance of the altered Raman spectrum depends on the quality of the contact between the first MoS<sub>2</sub> layer and Au, we suggest that in particular, the most mysterious A<sub>1g, reduced</sub> mode around 397 cm<sup>-1</sup> is related to the MoS<sub>2</sub>–Au interaction. Gong et al. predicted<sup>25</sup> that this interaction should cause mid gap states and thus Fermi level pinning by S-atom-mediated spreading of mainly the d-orbitals of the Mo atoms into the band gap. As a result, the Mo–S bond is weakened. In the harmonic oscillator model, bond weakening corresponds to a reduction of the spring constant and consequently a reduction of the frequency or Raman shift. In conclusion, the A<sub>1g, reduced</sub> mode around 397 cm<sup>-1</sup> can be interpreted as the common A<sub>1g</sub> mode with a reduced wavenumber. In order to prove that the A<sub>1g, reduced</sub> mode is indeed an A-type MoS<sub>2</sub> Raman mode, we performed polarization-dependent Raman spectroscopy on 1L-MoS<sub>2</sub> exfoliated on PVD-Au (inset of Figure 5b) and found that this mode behaves like the A<sub>1g</sub> mode, when changing from a parallel-polarized configuration (*xx*) to a cross-polarized configuration (*xy*).<sup>51</sup> In detail, the intensity of both modes, the A<sub>1g</sub> and A<sub>1g, reduced</sub> modes, vanishes in the cross-polarized configuration. We observe that the difference of the position of the A<sub>1g</sub> mode to the position of its reduced version A<sub>1g, reduced</sub> is constant for all Au substrates. From this, we can derive that the interaction strength is quantized: an interaction for one MoS<sub>2</sub> unit cell is either present or not. The intensity ratio A<sub>1g, reduced</sub>/A<sub>1g</sub> represents the ratio of MoS<sub>2</sub> areas interacting and not interacting with the Au surface and thus correlates with the density of gap states. Similar to spatial variations in the V<sub>CPD</sub> image, slight spatial inhomogeneities can be detected with averaging Raman mappings (see the Supporting



**Figure 6.** XPS spectra of 1L-MoS<sub>2</sub> and bulk-like MoS<sub>2</sub> exfoliated on Au. (a) Mo 3d doublet and the S 1s peak. (b) S 2p doublet. For 1L-MoS<sub>2</sub>, the peaks additionally split. Red line: cumulative fit. (c) Corresponding SXI and optical microscopy image.

Information, Figure S6), which further substantiates the correlation of the Fermi level and the altered Raman spectrum.

Note that we may discard a local variation of the doping as a cause for the A<sub>1g</sub> mode splitting (Figure 5) for the following reasons: (i) sign: from the doping dependence of the A<sub>1g</sub> mode, the A<sub>1g<sup>reduced</sup></sub> mode would qualitatively indicate a strongly n-doped MoS<sub>2</sub>.<sup>52</sup> Using KPFM, however, we find that exfoliated MoS<sub>2</sub> is on average significantly p-doped (a high work function) relative to CVD MoS<sub>2</sub> transferred onto PVD-Au (Figure 4b) which does not exhibit the A<sub>1g<sup>reduced</sup></sub> mode (Figure 5c or d). The comparison between MoS<sub>2</sub> exfoliated on PVD-Au and SC-Au even shows that the system with a higher A<sub>1g<sup>reduced</sup></sub>/A<sub>1g</sub> ratio (on average relatively n-doped) also has the higher work function (on average relatively p-doped). (ii) Quantity: applying the approach from the publication mentioned above,<sup>52</sup> the mode difference between the A<sub>1g</sub> and A<sub>1g<sup>reduced</sup></sub> modes would result in a local electron density difference on the order of  $3 \times 10^{13} \text{ cm}^{-2}$ . This would lead to very large electrostatic gradients, which prevent distinct doping areas as one would require for the interpretation of the sharp A-type Raman modes shown in Figure 5.

Next, we want to tackle the observation that only the A<sub>1g</sub> mode splits by the bond softening. For this, we start again with the prominent study of Chakraborty et al. on the dependence of doping and its influence on the MoS<sub>2</sub> modes mentioned previously.<sup>52</sup> It can be noted that as described above, almost only the A<sub>1g</sub> mode is sensitive to doping. Chakraborty et al. additionally explain this sensitivity based on simulations of different dependencies of the electron–phonon coupling for the E<sub>2g</sub><sup>1</sup> mode and A<sub>1g</sub> mode phonons, being due to the occupation of the bottom of the conduction band composed of the d-orbitals of the Mo atoms (e.g., due to electron doping). They show that the electron–phonon coupling for the E<sub>2g</sub><sup>1</sup> mode does not change, while for the A<sub>1g</sub> mode, it changes significantly. As in the MoS<sub>2</sub>-Au contact, according to Gong et al., the same Mo d-orbital states near the bottom of the conduction band move, in the Mo into the band gap and thus form the pinning gap states,<sup>25</sup> it is safe to assume that the occupation of the emerging gap states causes a very similar bond softening as in the case of doping and thus shifts in particular the A<sub>1g</sub> mode. The E<sub>2g</sub><sup>1</sup> mode splits only weakly (we estimate  $\sim 1 \text{ cm}^{-1}$  based on Chakraborty et al., which cannot be resolved sufficiently due to the peak width), corresponding to its weak dependence on doping.

The weakening of the Mo–S bond is further confirmed by our XPS measurements on 1L-MoS<sub>2</sub> and bulk-like MoS<sub>2</sub> on 25

nm PVD-Au. In Figure 6a,b, the S 2p and the Mo 3d doublets for MoS<sub>2</sub> are presented, respectively. Figure 6c shows the corresponding SXI (scanning X-ray-induced secondary electron image) with the two red spots indicating the measurement position of the 50 μm X-ray beam and the respective optical microscopy image. The XPS spectra of the bulk-like MoS<sub>2</sub> appear typical for non-defective MoS<sub>2</sub><sup>53</sup> for both the S 2p and Mo 3d signals. In contrast, the spectra for 1L-MoS<sub>2</sub> are shifted and show the existence of two different elemental species. In the case of the Mo 3d signal, the new doublet, shifted about 0.4 eV towards the lower binding energy side, makes up about 60% of the total Mo signal. The shift is somewhat smaller for the new doublet in the S 2p spectra with about 0.25 eV. Additionally, a shift of the S 2s signal is also observed. This shift might also be due to the existence of an additional S 2s signal. However, due to the low intensity of the S 2s peak, the two signals are indistinguishable. A shift to lower binding energies is attributed to a (partial) reduction of the oxidation state of the respective atoms and is thus in our case related to a bond weakening. The fact that only part of the intensity is shifted to lower binding energies indicates, similar to the Raman data, that only a fraction of the bonds are weakened. Note: the low oxygen content (<1 at. %) and the absence of the Mo 3d signal, which is related to Mo–O bonds, at both measured sites prove that the MoS<sub>2</sub> layers are not partially oxidized. Additional XPS data of the C 1s and O 1s peaks can be found in the Supporting Information, Figure S7.

In summary, we provide experimental evidence for the presence of metal-induced gap states due to the MoS<sub>2</sub>-Au interaction leading to the Fermi level pinning predicted by Gong et al.<sup>25</sup> From our KPFM data, using eq 2 and the electron affinity of  $\chi = 4.0\text{--}4.3 \text{ eV}$ , we can determine the Schottky barrier height for MoS<sub>2</sub> exfoliated on Au surfaces to be  $\phi_{\text{SBH}} = 0.53\text{--}1.02 \text{ eV}$ . This agrees well with calculations by Gong et al. and other groups predicting values in the range of  $0.76\text{--}0.88 \text{ eV}$ .<sup>25,28</sup> However, other experimental approaches yield different results. Lee et al. find  $\phi_{\text{SBH}} = 0.48 \pm 0.12 \text{ eV}$  by conductive AFM for MoS<sub>2</sub> exfoliated on template-stripped Au,<sup>46</sup> while experiments with MoS<sub>2</sub>-FETs yield values of only  $0.13\text{--}0.32 \text{ eV}$ .<sup>13,54</sup>

We believe that defects play an important role for this discrepancy. In particular, sulfur vacancies in MoS<sub>2</sub>-Au contacts shift the Fermi level toward the conduction band, thus reducing the Schottky barrier height.<sup>26</sup> Although the interface in our sample system is very similar to that in devices, there is one crucial difference: while the exfoliation on a pre-existing gold layer is very gentle, producing metallic contacts

by PVD is known to stress and damage 1L-MoS<sub>2</sub>.<sup>14</sup> Therefore, in real devices, larger defect densities in the contact area are expected and could account for the reduced  $\phi_{\text{SBH}}$ .

Finally, we would like to demonstrate that the exfoliation of single-layer MoS<sub>2</sub> on gold does indeed provide direct access to a metal–semiconductor interface as Raman spectroscopy can be used to characterize the buried MoS<sub>2</sub>–Au interface. To this end, we perform additional double-transmission backscattering Raman spectroscopy measurements. We deposited 5 nm Ti and 25 nm Au on a transparent double-side polished sapphire substrate, and subsequently, large-area 1L-MoS<sub>2</sub> was exfoliated onto the freshly prepared gold surface. The Raman spectroscopy measurements were now performed in an upside-down setup, that is, backscattered through the sapphire substrate and both metal layers (see the inset in Figure 7). As seen in Figure

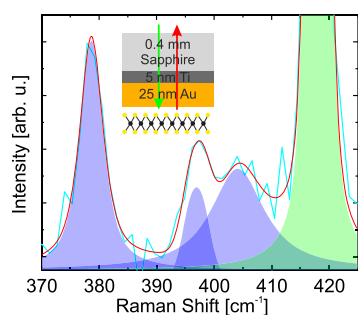


**Figure 7.** Double-transmission backscattering Raman spectroscopy. Even in this setup (see illustration in the inset), the unusual Raman signature of exfoliated 1L-MoS<sub>2</sub> interacting with the gold surface can still be identified (blue fits). Green fit: the Raman mode of the sapphire substrate. Red line: cumulative fit.

7, the unusual Raman signature (blue peak areas) can still be identified in the resulting spectra, although the intensity is reduced, which can partially be compensated by an extended integration time. As a consequence, conclusions drawn from the MoS<sub>2</sub>–Au system prepared and studied in this paper and in future experiments can be used to characterize real devices with buried interfaces if the corresponding information is related to the Raman signature. For example, the correlation of the  $A_{1\text{g}}^{\text{reduced}}/A_{1\text{g}}$  ratio with more limited methods as AFM/KPFM can be used for monitoring the interaction strength of the buried MoS<sub>2</sub>–Au interface.

## CONCLUSIONS

Two-dimensional MoS<sub>2</sub> is the prototypical 2D material for optoelectronic devices, and detailed knowledge of metal–semiconductor contacts is indispensable. However, the experimental characterization of a metal–semiconductor contact and its interface is a difficult task. We have demonstrated by Raman spectroscopy that mechanical exfoliation of MoS<sub>2</sub> onto a clean, PVD-grown Au surface yields a metal–semiconductor interface very similar to that in devices fabricated by the conventional evaporation techniques. Thus, it provides a novel way to study the Schottky barrier and related electronic changes at a device-relevant interface. The fabrication process is however crucial: we have shown that a simple (wet) transfer of MoS<sub>2</sub> onto the metal surface does not result in a metal–semiconductor junction comparable to real device structures. Instead, transferred MoS<sub>2</sub> layers are decoupled from the substrate by a contamination/water layer, possibly in a similar way to hBN buffer layers in

between MoS<sub>2</sub> and a metal contact.<sup>55–57</sup> In this case, the Schottky barrier based on Fermi level pinning is replaced with a tunnel barrier. Therefore, all data obtained from systems prepared in this way must be critically reviewed if conclusions about real devices are to be drawn.

In the exfoliated system studied here, the previously observed peculiar Raman spectrum is extremely pronounced, which has allowed us to investigate its origin. Through detailed analysis, we have shown that this anomalous Raman signature is indeed directly related to the contact strength between Au and MoS<sub>2</sub>. One of the modes, which has been unambiguously identified as the out-of-plane A-mode, can be interpreted as the result of a weakening of the bond between the S and Mo atoms related to metal-induced gap states and the resulting Fermi level pinning. The ratio between the additionally emerged mode  $A_{1\text{g}}^{\text{reduced}}$  and the original  $A_{1\text{g}}$  mode thus provides a measure of the degree of the contact strength and/or the contact area between MoS<sub>2</sub> and the gold surface. We suggest that this ratio derived from spectra of the rapid, non-destructive, and spatially resolved Raman spectroscopy is very useful to examine the cleanliness and the quality of the MoS<sub>2</sub>–Au interface. This is particularly relevant for dry stacked samples because the quality of their interfaces can exhibit strong spatial inhomogeneities as studies on dry stacked van der Waals heterostructures have shown.<sup>58,59</sup>

Given our findings that the 1L-MoS<sub>2</sub> work function depends on the area in direct contact with the Au substrate, it is likely that the previously observed reduction of contact resistance by introduction of energy or particles<sup>4,60–62</sup> is related to a shift of the Fermi level toward the conduction band, probably due to thermally induced sulfur vacancies at the interface. However, since any surface treatment can induce several changes not only at the interface but also at the MoS<sub>2</sub> surface<sup>63,64</sup> (see the Supporting Information, Figure S8, for 1L-MoS<sub>2</sub> on Au), further studies on this important topic are certainly needed, in particular because the origin of such treatment-mediated surface changes is not yet understood. The mechanical exfoliation of MoS<sub>2</sub> on fresh/clean Au substrates provides not only unusually large areas but also electrically well-contacted samples, without the need for polymer-based transfer or lithography steps. This approach thus ensures a low level of contaminations, and a much wider range of surface characterization techniques can be applied. Together with the pronounced MoS<sub>2</sub>–Au interaction, this results in an ideal system for further characterization of the metal–semiconductor interface and for elucidating phenomena like changes due to surface treatment.

We believe that our conclusions can also be applied to other transition-metal dichalcogenide-metal systems because for the MoS<sub>2</sub>–Ag and WS<sub>2</sub>–Ag/Au systems, similar features in the Raman signature have been observed.<sup>15–18</sup>

Note that since this paper has been submitted, a related study of the interaction of large-area exfoliated MoS<sub>2</sub> with its gold substrate has become available.<sup>65</sup>

## METHODS

**Sample Preparation. Large-Area Exfoliation.** Large-area exfoliation is basically the same as usual micromechanical exfoliation. The key for large-area exfoliation is the substrate, which has to be a clean Au surface. For this purpose, the Au surface was either freshly produced or sufficiently cleaned. The production of fresh Au surfaces was realized by PVD

techniques: Ti adhesive films by e-beam sputtering (growth rate 0.15 Å/s), Au films by thermal evaporation (growth rate 1 Å/s), PVD-chamber base pressure:  $1.5 \times 10^{-5}$  mbar. These metal layers are subsequently deposited on clean SiO<sub>2</sub>/Si or sapphire substrates, respectively. The Au(111) SC was cleaned in a UHV chamber (base pressure:  $10^{-9}$  mbar) by several cycles of sputtering (1.5 keV Ar<sup>+</sup>, 3 min) and subsequent annealing (800–850 K, 30 min). An X-ray diffraction pattern of 25 nm thick Au prepared by PVD is shown in the Supporting Information, Figure S2, revealing its crystallinity. Immediately after Au surface preparation and removal from the vacuum chamber, MoS<sub>2</sub> was exfoliated on both types of gold surfaces.

**Reference Samples.** Reference samples were prepared by (i) conventional exfoliation of MoS<sub>2</sub> on SiO<sub>2</sub> substrates, (ii) CVD of MoS<sub>2</sub> onto SiO<sub>2</sub>, and (iii) CVD growth of MoS<sub>2</sub> and subsequent transfer onto 25 nm PVD-Au. Both techniques, CVD and transfer, are common techniques and also reported in our previous study.<sup>40</sup>

More details of the sample preparation can be found in the Supporting Information, Figure S1.

**Characterization. AFM and KPFM.** AFM and KPFM were performed with a Dimension Icon (Bruker) in the PeakForce Tapping Mode and PeakForce KPFM Mode using ScanAsyst-Air and PFQNE-AL tips, respectively. The latter mode combines the Brukers PeakForce Tapping Mode with frequency-modulated KPFM in a dual-pass setup. The compensation voltage was applied to the sample; thus, the sample work function  $\phi_{\text{sample}}$  ( $\approx \phi_{\text{CNL}}$  in the case of 1L-MoS<sub>2</sub> on Au, as seen in Figure 1b) can be calculated by the following formula:  $\phi_{\text{sample}} = eV_{\text{CPD}} - \phi_{\text{tip}}$ . The tip was calibrated on a freshly cleaved highly oriented pyrolytic graphite crystal.

**Raman and PL.** Raman and PL measurements were performed with a Raman microscope (Renishaw InVia) with an excitation wavelength of  $\lambda = 532$  nm and a spot size of about 1  $\mu\text{m}$ . Polarization-dependent Raman spectra are recorded using a WITec Alpha300 RA Raman System with an excitation wavelength of  $\lambda = 532$  nm.

**X-ray Photoelectron Spectroscopy.** XPS measurements were performed using a VersaProbe II micro-focus X-ray photoelectron spectrometer (UlvacPhi).

## ■ ASSOCIATED CONTENT

### SI Supporting Information

The Supporting Information is available free of charge at <https://pubs.acs.org/doi/10.1021/acsomega.1c01570>.

MoS<sub>2</sub> on gold: details and illustration of the sample preparation, XRD pattern, AFM images revealing the PVD-Au morphology, additional KPFM images, optical microscopy images of the water intercalation for MoS<sub>2</sub> on 5 nm PVD-Au, Raman mappings revealing slight spatial inhomogeneities, additional XPS data (C 1s and O 1s), and Raman laser power density and integration time dependency of morphology and surface potential of MoS<sub>2</sub> on PVD-Au in comparison to PVD-Au (PDF)

## ■ AUTHOR INFORMATION

### Corresponding Author

Erik Pollmann – Faculty of Physics and CENIDE, University of Duisburg-Essen, D-47057 Duisburg, Germany;  
orcid.org/0000-0002-3961-0426;  
Email: erik.pollmann@uni-due.de

## Authors

Stephan Sleziona – Faculty of Physics and CENIDE, University of Duisburg-Essen, D-47057 Duisburg, Germany

Tobias Foller – Faculty of Physics and CENIDE, University of Duisburg-Essen, D-47057 Duisburg, Germany; Present Address: School of Materials Science and Engineering, University of New South Wales, AUS-2052 Sydney, Australia.; orcid.org/0000-0003-2636-4542

Ulrich Hagemann – ICAN and CENIDE, University of Duisburg-Essen, D-47057 Duisburg, Germany; orcid.org/0000-0002-1880-6550

Claudia Gorynski – Faculty of Engineering and CENIDE, University Duisburg-Essen, D-47057 Duisburg, Germany

Oliver Petri – Faculty of Physics and CENIDE, University of Duisburg-Essen, D-47057 Duisburg, Germany

Lukas Madauß – Faculty of Physics and CENIDE, University of Duisburg-Essen, D-47057 Duisburg, Germany; orcid.org/0000-0003-2556-5967

Lars Breuer – Faculty of Physics and CENIDE, University of Duisburg-Essen, D-47057 Duisburg, Germany; orcid.org/0000-0002-7797-9662

Marika Schleberger – Faculty of Physics and CENIDE, University of Duisburg-Essen, D-47057 Duisburg, Germany; orcid.org/0000-0002-5785-1186

Complete contact information is available at: <https://pubs.acs.org/doi/10.1021/acsomega.1c01570>

## Notes

The authors declare no competing financial interest.

## ■ ACKNOWLEDGMENTS

The authors gratefully acknowledge support from the German Research Foundation (DFG) by funding SCHL 384/20-1 (project number 406129719) and project C5 within the SFB1242 “Non-Equilibrium Dynamics of Condensed Matter in the Time Domain” (project number 278162697). This work has been supported by the Interdisciplinary Center for Analytics on the Nanoscale (ICAN), a core facility funded by the DFG (reference RI\_00313). The authors particularly acknowledge the cleanroom team (Dennis Oing, Nicolas Wöhrl, and Günther Prinz) of the Prof. Axel Lorke research group. The authors acknowledge support by the Open Access Publication Fund of the University of Duisburg-Essen.

## ■ ABBREVIATIONS

1L-MoS<sub>2</sub>, single-layer molybdenum disulfide; 2D, two-dimensional; FET, field-effect transistor; SBH, Schottky barrier height; CNL, charge neutrality level;  $V_{\text{CPD}}$ , contact potential difference; AFM, atomic force microscopy; KPFM, Kelvin probe force microscopy; XPS, X-ray photoelectron spectroscopy; PL, photoluminescence; PVD, physical vapor deposition; SC, single crystal; CVD, chemical vapor deposition

## ■ REFERENCES

- (1) Splendiani, A.; Sun, L.; Zhang, Y.; Li, T.; Kim, J.; Chim, C.-Y.; Galli, G.; Wang, F. Emerging Photoluminescence in Monolayer MoS<sub>2</sub>. *Nano Lett.* **2010**, *10*, 1271–1275.
- (2) Mak, K. F.; Lee, C.; Hone, J.; Shan, J.; Heinz, T. F. Atomically Thin MoS<sub>2</sub>: a New Direct-Gap Semiconductor. *Phys. Rev. Lett.* **2010**, *105*, 136805.
- (3) Kuc, A.; Zibouche, N.; Heine, T. Influence of Quantum Confinement on the Electronic Structure of the Transition Metal

Sulfide TS<sub>2</sub>. *Phys. Rev. B: Condens. Matter Mater. Phys.* **2011**, *83*, 245213.

(4) Radisavljevic, B.; Radenovic, A.; Brivio, J.; Giacometti, V.; Kis, A. Single-Layer MoS<sub>2</sub> Transistors. *Nat. Nanotechnol.* **2011**, *6*, 147–150.

(5) Li, H.; Yin, Z.; He, Q.; Li, H.; Huang, X.; Lu, G.; Fam, D. W. H.; Tok, A. I. Y.; Zhang, Q.; Zhang, H. Fabrication of Single- and Multilayer MoS<sub>2</sub> Film-Based Field-Effect Transistors for Sensing NO at Room Temperature. *Small* **2012**, *8*, 63–67.

(6) Lopez-Sanchez, O.; Lembke, D.; Kayci, M.; Radenovic, A.; Kis, A. Ultrasensitive Photodetectors Based on Monolayer MoS<sub>2</sub>. *Nat. Nanotechnol.* **2013**, *8*, 497–501.

(7) Late, D. J.; Huang, Y.-K.; Liu, B.; Acharya, J.; Shirodkar, S. N.; Luo, J.; Yan, A.; Charles, D.; Waghmare, U. V.; Dravid, V. P.; et al. Sensing Behavior of Atomically Thin-Layered MoS<sub>2</sub> Transistors. *ACS Nano* **2013**, *7*, 4879–4891.

(8) Di Bartolomeo, A.; Genovese, L.; Foller, T.; Giubileo, F.; Luongo, G.; Croin, L.; Liang, S.-J.; Ang, L. K.; Schleberger, M. Electrical Transport and Persistent Photoconductivity in Monolayer MoS<sub>2</sub> Phototransistors. *Nanotechnology* **2017**, *28*, 214002.

(9) Lee, J.; Pak, S.; Lee, Y.-W.; Cho, Y.; Hong, J.; Giraud, P.; Shin, H. S.; Morris, S. M.; Sohn, J. I.; Cha, S.; et al. Monolayer Optical Memory Cells Based on Artificial Trap-Mediated Charge Storage and Release. *Nat. Commun.* **2017**, *8*, 14734.

(10) Di Bartolomeo, A.; Genovese, L.; Giubileo, F.; Iemmo, L.; Luongo, G.; Foller, T.; Schleberger, M. Hysteresis in the Transfer Characteristics of MoS<sub>2</sub> Transistors. *2D Mater.* **2018**, *5*, 015014.

(11) Urban, F.; Giubileo, F.; Grillo, A.; Iemmo, L.; Luongo, G.; Passacantando, M.; Foller, T.; Madauß, L.; Pollmann, E.; Geller, M. P.; et al. Gas Dependent Hysteresis in MoS<sub>2</sub> Field Effect Transistors. *2D Mater.* **2019**, *6*, 045049.

(12) Robertson, J. Band Offsets, Schottky Barrier Heights, and Their Effects on Electronic Devices. *J. Vac. Sci. Technol., A* **2013**, *31*, 050821.

(13) Kim, C.; Moon, I.; Lee, D.; Choi, M. S.; Ahmed, F.; Nam, S.; Cho, Y.; Shin, H.-J.; Park, S.; Yoo, W. J. Fermi Level Pinning at Electrical Metal Contacts of Monolayer Molybdenum Dichalcogenides. *ACS Nano* **2017**, *11*, 1588–1596.

(14) Liu, Y.; Guo, J.; Zhu, E.; Liao, L.; Lee, S.-J.; Ding, M.; Shakir, I.; Gambin, V.; Huang, Y.; Duan, X. Approaching the Schottky-Mott Limit in van der Waals Metal-Semiconductor Junctions. *Nature* **2018**, *557*, 696–700.

(15) Gong, C.; Huang, C.; Miller, J.; Cheng, L.; Hao, Y.; Cobden, D.; Kim, J.; Ruoff, R. S.; Wallace, R. M.; Cho, K.; et al. Metal Contacts on Physical Vapor Deposited Monolayer MoS<sub>2</sub>. *ACS Nano* **2013**, *7*, 11350–11357.

(16) Sun, Y.; Liu, K.; Hong, X.; Chen, M.; Kim, J.; Shi, S.; Wu, J.; Zettl, A.; Wang, F. Probing Local Strain at MX<sub>2</sub>-Metal Boundaries with Surface Plasmon-Enhanced Raman Scattering. *Nano Lett.* **2014**, *14*, 5329–5334.

(17) Zhang, D.; Wu, Y.-C.; Yang, M.; Liu, X.; Coileáin, C. Ó.; Abid, M.; Abid, M.; Wang, J.-J.; Shvets, I.; Xu, H.; et al. Surface Enhanced Raman Scattering of Monolayer MX<sub>2</sub> with Metallic Nano Particles. *Sci. Rep.* **2016**, *6*, 30320.

(18) Zhao, W.; Wu, Q.; Hao, Q.; Wang, J.; Li, M.; Zhang, Y.; Bi, K.; Chen, Y.; Ni, Z. Plasmon-Phonon Coupling in Monolayer WS<sub>2</sub>. *Appl. Phys. Lett.* **2016**, *108*, 131903.

(19) Lee, C.; Yan, H.; Brus, L. E.; Heinz, T. F.; Hone, J.; Ryu, S. Anomalous Lattice Vibrations of Single- and Few-Layer MoS<sub>2</sub>. *ACS Nano* **2010**, *4*, 2695–2700.

(20) Rice, C.; Young, R. J.; Zan, R.; Bangert, U.; Wolverson, D.; Georgiou, T.; Jalil, R.; Novoselov, K. S. Raman-Scattering Measurements and First-Principles Calculations of Strain-Induced Phonon Shifts in Monolayer MoS<sub>2</sub>. *Phys. Rev. B: Condens. Matter Mater. Phys.* **2013**, *87*, 081307.

(21) Wang, Y.; Cong, C.; Qiu, C.; Yu, T. Raman Spectroscopy Study of Lattice Vibration and Crystallographic Orientation of Monolayer MoS<sub>2</sub> under Uniaxial Strain. *Small* **2013**, *9*, 2857–2861.

(22) Conley, H. J.; Wang, B.; Ziegler, J. I.; Haglund, R. F.; Pantelides, S. T.; Bolotin, K. I. Bandgap Engineering of Strained Monolayer and Bilayer MoS<sub>2</sub>. *Nano Lett.* **2013**, *13*, 3626–3630.

(23) Popov, I.; Seifert, G.; Tománek, D. Designing Electrical Contacts to MoS<sub>2</sub> Monolayers: a Computational Study. *Phys. Rev. Lett.* **2012**, *108*, 156802.

(24) Chen, W.; Santos, E. J. G.; Zhu, W.; Kaxiras, E.; Zhang, Z. Tuning the Electronic and Chemical Properties of Monolayer MoS<sub>2</sub> Adsorbed on Transition Metal Substrates. *Nano Lett.* **2013**, *13*, 509–514.

(25) Gong, C.; Colombo, L.; Wallace, R. M.; Cho, K. The Unusual Mechanism of Partial Fermi Level Pinning at Metal-MoS<sub>2</sub> Interfaces. *Nano Lett.* **2014**, *14*, 1714–1720.

(26) Su, J.; Li, N.; Zhang, Y.; Feng, L.; Liu, Z. Role of Vacancies in Tuning the Electronic Properties of Au-MoS<sub>2</sub> Contact. *AIP Adv.* **2015**, *5*, 077182.

(27) Guo, Y.; Liu, D.; Robertson, J. 3D Behavior of Schottky Barriers of 2D Transition-Metal Dichalcogenides. *ACS Appl. Mater. Interfaces* **2015**, *7*, 25709–25715.

(28) Zhong, H.; Quhe, R.; Wang, Y.; Ni, Z.; Ye, M.; Song, Z.; Pan, Y.; Yang, J.; Yang, L.; Lei, M.; et al. Interfacial Properties of Monolayer and Bilayer MoS<sub>2</sub> Contacts with Metals: Beyond the Energy Band Calculations. *Sci. Rep.* **2016**, *6*, 21786.

(29) Min, K.-A.; Park, J.; Wallace, R. M.; Cho, K.; Hong, S. Reduction of Fermi Level Pinning at Au–MoS<sub>2</sub> Interfaces by Atomic Passivation on Au Surface. *2D Mater.* **2017**, *4*, 015019.

(30) Magda, G. Z.; Pető, J.; Dobrik, G.; Hwang, C.; Biró, L. P.; Tapasztó, L. Exfoliation of Large-Area Transition Metal Chalcogenide Single Layers. *Sci. Rep.* **2015**, *5*, 14714.

(31) Velický, M.; Donnelly, G. E.; Hendren, W. R.; McFarland, S.; Scullion, D.; DeBenedetti, W. J. I.; Correa, G. C.; Han, Y.; Wain, A. J.; Hines, M. A.; et al. Mechanism of Gold-Assisted Exfoliation of Centimeter-Sized Transition-Metal Dichalcogenide Monolayers. *ACS Nano* **2018**, *12*, 10463–10472.

(32) Pető, J.; Dobrik, G.; Kukucska, G.; Vancsó, P.; Koós, A. A.; Koltai, J.; Nemes-Incze, P.; Hwang, C.; Tapasztó, L. Moderate Strain Induced Indirect Bandgap and Conduction Electrons in MoS<sub>2</sub> Single Layers. *npj 2D Mater. Appl.* **2019**, *3*, 39.

(33) Jain, S. C.; Kirshnan, K. S. The Thermionic Constants of Metals and Semi-Conductors I. Graphite. *Proc. R. Soc. A* **1952**, *213*, 143–157.

(34) Ochedowski, O.; Marinov, K.; Scheuschner, N.; Poloczek, A.; Bussmann, B. K.; Maultzsch, J.; Schleberger, M. Effect of Contaminations and Surface Preparation on the Work Function of Single Layer MoS<sub>2</sub>. *Beilstein J. Nanotechnol.* **2014**, *5*, 291–297.

(35) Robinson, B. J.; Giusca, C. E.; Gonzalez, Y. T.; Kay, N. D.; Kazakova, O.; Kolosov, O. V. Structural, Optical and Electrostatic Properties of Single and Few-Layers MoS<sub>2</sub>: Effect of Substrate. *2D Mater.* **2015**, *2*, 015005.

(36) Kim, J. H.; Lee, J.; Kim, J. H.; Hwang, C. C.; Lee, C.; Park, J. Y. Work Function Variation of MoS<sub>2</sub> Atomic Layers Grown with Chemical Vapor Deposition: The Effects of Thickness and the Adsorption of Water/Oxygen Molecules. *Appl. Phys. Lett.* **2015**, *106*, 251606.

(37) Sohn, A.; Moon, H.; Kim, J.; Seo, M.; Min, K.-A.; Lee, S. W.; Yoon, S.; Hong, S.; Kim, D.-W. Band Alignment at Au/MoS<sub>2</sub> Contacts: Thickness Dependence of Exfoliated Flakes. *J. Phys. Chem. C* **2017**, *121*, 22517–22522.

(38) Tamulewicz, M.; Kutrowska-Girzycka, J.; Gajewski, K.; Serafińczuk, J.; Sierakowski, A.; Jadcak, J.; Bryja, L.; Gotszalk, T. P. Layer Number Dependence of the Work Function and Optical Properties of Single and Few Layers MoS<sub>2</sub>: Effect of Substrate. *Nanotechnology* **2019**, *30*, 245708.

(39) Pollmann, E.; Morbec, J. M.; Madauß, L.; Bröckers, L.; Kratzer, P.; Schleberger, M. Molybdenum Disulfide Nanoflakes Grown by Chemical Vapor Deposition on Graphite: Nucleation, Orientation, and Charge Transfer. *J. Phys. Chem. C* **2020**, *124*, 2689–2697.

(40) Pollmann, E.; Madauß, L.; Schumacher, S.; Kumar, U.; Heuvel, F.; vom Ende, C.; Yilmaz, S.; Güngörmüş, S.; Schleberger, M.

Apparent Differences between Single Layer Molybdenum Disulfide Fabricated via Chemical Vapor Deposition and Exfoliation. *Nanotechnology* **2020**, *31*, 505604.

(41) Shi, Y.; Huang, J.-K.; Jin, L.; Hsu, Y.-T.; Yu, S. F.; Li, L.-J.; Yang, H. Y. Selective Decoration of Au Nanoparticles on Monolayer MoS<sub>2</sub> Single Crystals. *Sci. Rep.* **2013**, *3*, 1839.

(42) Kim, E.; Lee, Y.; Ko, C.; Park, Y.; Yeo, J.; Chen, Y.; Choe, H. S.; Allen, F. I.; Rho, J.; Tongay, S.; et al. Tuning the Optical and Electrical Properties of MoS<sub>2</sub> by Selective Ag Photo-Reduction. *Appl. Phys. Lett.* **2018**, *113*, 013105.

(43) Bhanu, U.; Islam, M. R.; Tetard, L.; Khondaker, S. I. Photoluminescence Quenching in Gold-MoS<sub>2</sub> Hybrid Nanoflakes. *Sci. Rep.* **2014**, *4*, 5575.

(44) Kang, J.; Tongay, S.; Zhou, J.; Li, J.; Wu, J. Band Offsets and Heterostructures of Two-Dimensional Semiconductors. *Appl. Phys. Lett.* **2013**, *102*, 012111.

(45) Tangi, M.; Mishra, P.; Li, M.-Y.; Shakfa, M. K.; Anjum, D. H.; Hedhili, M. N.; Ng, T. K.; Li, L.-J.; Ooi, B. S. Type-I Band Alignment at MoS<sub>2</sub>/In<sub>0.15</sub>Al<sub>0.85</sub>N Lattice Matched Heterojunction and Realization of MoS<sub>2</sub> Quantum Well. *Appl. Phys. Lett.* **2017**, *111*, 092104.

(46) Lee, H.; Deshmukh, S.; Wen, J.; Costa, V. Z.; Schuder, J. S.; Sanchez, M.; Ichimura, A. S.; Pop, E.; Wang, B.; Newaz, A. K. M. Layer-Dependent Interfacial Transport and Optoelectrical Properties of MoS<sub>2</sub> on Ultraflat Metals. *ACS Appl. Mater. Interfaces* **2019**, *11*, 31543–31550.

(47) Mignuzzi, S.; Pollard, A. J.; Bonini, N.; Brennan, B.; Gilmore, I. S.; Pimenta, M. A.; Richards, D.; Roy, D. Effect of Disorder on Raman Scattering of Single-Layer MoS<sub>2</sub>. *Phys. Rev. B: Condens. Matter Mater. Phys.* **2015**, *91*, 195411.

(48) He, Z.; Zhao, R.; Chen, X.; Chen, H.; Zhu, Y.; Su, H.; Huang, S.; Xue, J.; Dai, J.; Cheng, S.; et al. Defect Engineering in Single-Layer MoS<sub>2</sub> Using Heavy Ion Irradiation. *ACS Appl. Mater. Interfaces* **2018**, *10*, 42524–42533.

(49) Parkin, W. M.; Balan, A.; Liang, L.; Das, P. M.; Lamparski, M.; Naylor, C. H.; Rodríguez-Manzo, J. A.; Johnson, A. T. C.; Meunier, V.; Drndić, M. Raman Shifts in Electron-Irradiated Monolayer MoS<sub>2</sub>. *ACS Nano* **2016**, *10*, 4134–4142.

(50) Bampoulis, P.; van Bremen, R.; Yao, Q.; Poelsema, B.; Zandvliet, H. J. W.; Soththwes, K. Defect Dominated Charge Transport and Fermi Level Pinning in MoS<sub>2</sub>/Metal Contacts. *ACS Appl. Mater. Interfaces* **2017**, *9*, 19278–19286.

(51) Wieting, T. J.; Verble, J. L. Infrared and Raman Studies of Long-Wavelength Optical Phonons in Hexagonal MoS<sub>2</sub>. *Phys. Rev. B: Solid State* **1971**, *3*, 4286–4292.

(52) Chakraborty, B.; Bera, A.; Muthu, D. V. S.; Bhowmick, S.; Waghmare, U. V.; Sood, A. K. Symmetry-Dependent Phonon Renormalization in Monolayer MoS<sub>2</sub> Transistor. *Phys. Rev. B: Condens. Matter Mater. Phys.* **2012**, *85*, 161403.

(53) Ganta, D.; Sinha, S.; Haasch, R. T. 2-D Material Molybdenum Disulfide Analyzed by XPS. *Surf. Sci. Spectra* **2014**, *21*, 19–27.

(54) Kaushik, N.; Nipane, A.; Basheer, F.; Dubey, S.; Grover, S.; Deshmukh, M. M.; Lodha, S. Schottky Barrier Heights for Au and Pd Contacts to MoS<sub>2</sub>. *Appl. Phys. Lett.* **2014**, *105*, 113505.

(55) Farmanbar, M.; Brocks, G. Controlling the Schottky Barrier at MoS<sub>2</sub>/Metal Contacts by Inserting a BN Monolayer. *Phys. Rev. B: Condens. Matter Mater. Phys.* **2015**, *91*, 161304.

(56) Farmanbar, M.; Brocks, G. Ohmic Contacts to 2D Semiconductors through van der Waals Bonding. *Adv. Electron. Mater.* **2016**, *2*, 1500405.

(57) Cui, X.; Shih, E.-M.; Jauregui, L. A.; Chae, S. H.; Kim, Y. D.; Li, B.; Seo, D.; Pistunova, K.; Yin, J.; Park, J.-H.; et al. Low-Temperature Ohmic Contact to Monolayer MoS<sub>2</sub> by van der Waals Bonded Co/h-BN Electrodes. *Nano Lett.* **2017**, *17*, 4781–4786.

(58) Froehlicher, G.; Lorchat, E.; Bercaud, S. Charge Versus Energy Transfer in Atomically Thin Graphene-Transition Metal Dichalcogenide van der Waals Heterostructures. *Phys. Rev. X* **2018**, *8*, 011007.

(59) Yang, B.; Molina, E.; Kim, J.; Barroso, D.; Lohmann, M.; Liu, Y.; Xu, Y.; Wu, R.; Bartels, L.; Watanabe, K.; et al. Effect of Distance on Photoluminescence Quenching and Proximity-Induced Spin-Orbit

Coupling in Graphene/WSe<sub>2</sub> Heterostructures. *Nano Lett.* **2018**, *18*, 3580–3585.

(60) Baugher, B. W. H.; Churchill, H. O. H.; Yang, Y.; Jarillo-Herrero, P. Intrinsic Electronic Transport Properties of High-Quality Monolayer and Bilayer MoS<sub>2</sub>. *Nano Lett.* **2013**, *13*, 4212–4216.

(61) Kwon, H.; Baik, S.; Jang, J.; Jang, J.; Kim, S.; Grigoropoulos, C.; Kwon, H.-J. Ultra-Short Pulsed Laser Annealing Effects on MoS<sub>2</sub> Transistors with Asymmetric and Symmetric Contacts. *Electronics* **2019**, *8*, 222.

(62) Pelella, A.; Kharsah, O.; Grillo, A.; Urban, F.; Passacantando, M.; Giubileo, F.; Iemmo, L.; Sleziona, S.; Pollmann, E.; Madauß, L.; et al. Electron Irradiation of Metal Contacts in Monolayer MoS<sub>2</sub> Field Effect Transistors. *ACS Appl. Mater. Interfaces* **2020**, *12*, 40532–40540.

(63) Tran Khac, B. C.; Jeon, K.-J.; Choi, S. T.; Kim, Y. S.; DelRio, F. W.; Chung, K.-H. Laser-Induced Particle Adsorption on Atomically Thin MoS<sub>2</sub>. *ACS Appl. Mater. Interfaces* **2016**, *8*, 2974–2984.

(64) Alrasheed, A.; Gorham, J. M.; Tran Khac, B. C.; Alsaffar, F.; DelRio, F. W.; Chung, K.-H.; Amer, M. R. Surface Properties of Laser-Treated Molybdenum Disulfide Nanosheets for Optoelectronic Applications. *ACS Appl. Mater. Interfaces* **2018**, *10*, 18104–18112.

(65) Velický, M.; Rodríguez, A.; Bouša, M.; Krayev, A. V.; Vondráček, M.; Honolka, J.; Ahmadi, M.; Donnelly, G. E.; Huang, F.; Abruña, H. D.; et al. Strain and Charge Doping Fingerprints of the Strong Interaction between Monolayer MoS<sub>2</sub> and Gold. *J. Phys. Chem. Lett.* **2020**, *11*, 6112–6118.

# DuEPublico

Duisburg-Essen Publications online

UNIVERSITÄT  
DUISBURG  
ESSEN

*Offen im Denken*

ub | universitäts  
bibliothek

This text is made available via DuEPublico, the institutional repository of the University of Duisburg-Essen. This version may eventually differ from another version distributed by a commercial publisher.

**DOI:** 10.1021/acsomega.1c01570

**URN:** urn:nbn:de:hbz:465-20220310-104456-8



This work may be used under a Creative Commons Attribution - NonCommercial - NoDerivatives 4.0 License (CC BY-NC-ND 4.0).